Research Paper

Interface reconstruction of adhering droplets for distortion correction using color-coded glare points and deep learning

Maximilian Dreisbach [a][ID],[*], Itzel Hinojos [a], Jochen Kriegseis [a][ID], Alexander Stroh [a][ID], Sebastian Burgmann [b][ID]

[a] *Institute of Fluids Mechanics (ISTM), Karlsruhe Institute of Technology (KIT), Kaiserstraße 10, 76131 Karlsruhe, Germany*
[b] *Chair of Fluid Mechanics, University of Wuppertal, Gaußstraße 20, 42119 Wuppertal, Germany*

ARTICLE INFO

ABSTRACT

The flow within adhering droplets subjected to external shear flows influences their stability and eventual detachment. Particle image velocimetry (PIV) is commonly used to measure the internal velocity fields, but requires distortion correction to account for refraction at the curved gas–liquid interface. Currently available correction methods based on ray tracing are limited to low external flow velocities and insignificant interface deformations. However, an extension to arbitrarily deformed droplet shapes is feasible if the instantaneous three-dimensional interface shape can be acquired. In the present work, a gas–liquid interface reconstruction by means of deep learning is applied to determine the instantaneous interface of adhering droplets in external shear flows. In this regard, an optical measurement technique based on the shadowgraphy method is employed that encodes additional three-dimensional (3D) information of the interface into the images via color-coded glare points from lateral light sources. On the basis of the images recorded in the experiments, the volumetric shape of the droplet is reconstructed by a neural network trained on the spatio-temporal interface dynamics from a synthetic dataset obtained by numerical simulation. The results of experiments with adhering droplets at different external flow velocities demonstrate that the combination of the learned droplet geometry with the depth encoding through the color-coded glare points facilitates a robust and flexible reconstruction. The proposed method reconstructs the instantaneous three-dimensional interface of adhering droplets at both high resolution and spatial accuracy and thereby enables the distortion correction of PIV measurements also at high external flow velocities.

1. Introduction

The internal flow within droplets or bubbles plays an important role in numerous different multiphase flow phenomena, such as droplet dispersing, adhering droplets subjected to external flows, the evaporation or freezing of droplets, and bubble flow among others. Particle image velocimetry (PIV) is commonly employed in the investigation of multiphase flows to reveal internal flows. Karlsson et al. (2019) used PIV to visualize the flow patterns and measure velocities inside freezing droplets. The authors found that Marangoni effects, which arise due to temperature differences in and around the droplet during freezing, induce a flow inside the droplet. Kinoshita et al. (2007) revealed the complex three-dimensional circulation patterns within a moving droplet in a microchannel using micro-PIV. Later, Duxenneuner et al. (2014) investigated the flow inside and around a droplet during liquid–liquid dispersion using micro-PIV and revealed the existence of a flow inside the droplet in main flow direction as well as a vortex

flow around the droplet. By means of PIV measurements Minor et al. (2009) and later Burgmann et al. (2021) have found that there is a complex interaction between the internal and external flow of adhering droplets, that is dependent on interface tension and the oscillation of both phases.

Adhering droplets in external flows occur in many technical applications, for instance in cleaning and drying processes (Thoreau et al., 2006; Seevaratnam et al., 2010), oil recovery (Thompson, 1994; Schleizer and Bonnecaze, 1999; Gupta and Basu, 2008; Madani and Amirfazli, 2014), heat exchangers (Korte and Jacobi, 2001; Kandlikar and Steinke, 2002; Wang et al., 2022), airfoil icing prevention (Karlsson et al., 2019) and in fuel cells, where a removal of the droplets is crucial for an efficient operation (Theodorakakos et al., 2006; Kumbur et al., 2006; Esposito et al., 2010; Burgmann et al., 2013). The flow around the droplet eventually leads to a detachment of the droplet from the solid surface at critical conditions, which occur when the external

---

* Corresponding author.
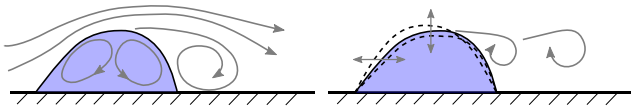 *E-mail address:* maximilian.dreisbach@kit.edu (M. Dreisbach).

Fig. 1. Visualization of an adhering droplet subjected to an external shear flow; time-averaged flow topology inside the droplet and in the external flow (left), droplet and flow oscillation (right).
Source: Figure adapted from Burgmann et al. (2021).

forces acting on the droplet become greater than the adhesion of the liquid droplet to the surface (Fan et al., 2011; Fu et al., 2014; Barwari et al., 2019; Burgmann et al., 2021). Several investigations have revealed an intricate interaction of the droplet with the surrounding flow. The droplet deforms (Gupta and Basu, 2008; Seevaratnam et al., 2010; Barwari et al., 2018) and additionally oscillates, when subjected to external shear flows (Zhi-yong et al., 2006; Burgmann et al., 2018b). It was shown that the contact angle hysteresis of the substrate and the droplet volume have an influence on the critical velocity for droplet detachment (Dussan, 1987; Kumbur et al., 2006; Barwari et al., 2019).

Previous investigations based on PIV-measurements revealed that the internal flow within the droplet is relevant to understanding the mechanism of droplet detachment. It was found that the internal flow follows the main flow direction of the external flow (Duxenneuner et al., 2009) and exhibits a clockwise rotational flow pattern (Minor et al., 2009). Minor et al. (2009) deduced that the secondary flow inside a droplet is induced by shear forces on the interface resulting from the external flow. Burgmann et al. (2018b,a) confirmed the findings of a clockwise vortex at low external flow velocities but also found an additional counterclockwise rotation at higher flow velocity that becomes dominant when approaching the critical velocity. Furthermore, the authors found an oscillation of the droplet with increasing amplitude toward higher external flow velocities. Burgmann et al. (2021) proposed that the droplet detachment is associated with a self-excitation process resulting from the oscillation of the gas–liquid interface, as well as the oscillation of the inner flow structure and the flow field around the droplet. The authors demonstrated that an emerging backflow region at higher external flow velocities induces the change in the flow pattern within the droplet and that the wake flow oscillates with the same frequency as the droplet. Later, Burgmann et al. (2022) found that the coupling of the internal and external flow leads to increased flow separation in comparison to rigid bodies and, consequently, a higher pressure force driving droplet detachment. Bilsing et al. (2025) measured the internal three-dimensional (3D) flow field by means of microscopic particle tracking velocimetry (PTV) through a transparent substrate from below and thereby revealed that the internal flow topology consists of multiple 3D vortical structures that change drastically depending on the external flow velocity. In experiments with rigid droplet models, Zhang et al. (2021) found that the external flow topology is significantly influenced by the shape of the adhering droplet. Consequently, a better understanding of the droplet deformation is required for any future investigation of the external flow. A visualization of the flow phenomena inside and around the droplet is shown in Fig. 1. The mutual dependence of wake flow, contour oscillation, and internal flow structure influences the stability of the droplet and eventually leads to the detachment of the droplet at critical conditions. While there has been significant scientific progress in recent years, the exact mechanism of droplet detachment still remains to be fully understood. Therefore, further experiments are required to obtain a better analytical model of droplet stability that accounts for aeroelastic effects and, consequently, allows for a more accurate prediction of the onset of droplet motion.

Despite the extensive use of PIV and micro-PIV measurements for the investigation of multiphase flows it is well known that refraction at the curved gas–liquid interfaces causes a distortion of the measured velocity fields (Karlsson et al., 2019; Kang et al., 2004; Minor et al.,

2007). The gas–liquid interface acts as a convex lens that refracts the light that is emitted from seeded particles within the droplet, which are illuminated by a light sheet (Kang et al., 2004). The refraction at different incident angles along the curved interface leads to a spatially inhomogeneous distortion, characterized by a large magnification in the center and an increasing warping toward the contour of the droplet. As a consequence, the topology of the internal flow is represented falsely in uncorrected PIV measurements. While a measurement from below avoids the distortion by the curved interface of the droplet (Bilsing et al., 2025), most substrates of interest for the technical application are optically opaque and, therefore, inaccessible by this method. Kang et al. (2004) and later Minor et al. (2007) developed a method for distortion correction that employs ray tracing to derive a mapping function between the image plane and the object plane, i.e. the illuminated particles in the light sheet. This mapping function can be applied to the PIV images or the measured velocity fields directly to reverse the distortion and thereby significantly increase the accuracy of the measurement.

In the method introduced by Kang et al. (2004) the contour of the droplet is detected from shadowgraph images and, subsequently, the three-dimensional droplet interface is obtained under the assumption of axisymmetry. To derive the mapping function between the image plane and the object plane, normally incident light rays on the image plane are traced to the droplet's interface, where the refraction is calculated by Snell's law. Through this method up to 80% of the internal flow field can be retrieved successfully, depending on the relative refractive indices of the considered fluids. Close to the contour, the retrieval of light from within the droplet is inhibited by total internal reflection and, consequently, the velocity field cannot be measured in these regions. Minor et al. (2009) demonstrated the applicability of the ray-tracing correction for micro-PIV measurements of the internal velocity field within an adhering droplet subjected to an external flow. Due to drag forces acting on the gas–liquid interface, the shape of the droplet deviates significantly from the assumed axisymmetrical shape. The authors stated that adaptive droplet shape approximations are required to reach a higher degree of accuracy for the deformed droplet shape. Burgmann et al. (2022) further underlined that the oscillating contour of adhering droplets at higher external flow velocities hinders an application of the ray-tracing method. A possible solution for the correction of the dynamic aberration by means of adaptive optics was recently introduced by Bilsing et al. (2024). This method, however, relies on a sophisticated optical system and has been tested only for a relatively flat droplet and low oscillation amplitude so far. Conversely, the ray-tracing method for distortion correction can be expanded straightforwardly to arbitrary droplet shapes, if the instantaneous three-dimensional shape of the gas–liquid interface can be acquired. Therefore, the reconstruction of the 3D interface in connection with laser-optical flow measurements inside the drop represents the next step toward gaining a deeper understanding of the internal flow and detachment process of adhering droplets.

For the volumetric reconstruction of interfaces in two-phase flows, various methods based on different optical measurement techniques have been proposed. Moreover, reconstruction algorithms can be broadly categorized into physics-based methods using analytical models, multi-view methods, and data-driven methods. Higashine et al. (2008) reconstructed the 3D gas–liquid interface shape of droplets deformed by gravitational or centrifugal forces through an analytical model based on the three-dimensional Laplace equation. Further analytical models considering the balance between gravitational and surface tension forces (Furmidge, 1962; Extrand and Kumagai, 1995; ElSherbini and Jacobi, 2004) and the minimization of total free energy (Carre and Shanahan, 1995) were proposed. While such analytical models reach a good agreement with experimental results, only the equilibrium state is considered, thus limiting their application to static droplets or those in uniform motion. Furthermore, most analytical

models require an accurate measurement of the advancing and receding contact angles. For bubbles with limited deformation, the shape of the gas–liquid interface can be approximated as an ellipsoid and reconstructed by fitting shadowgraphy contours in one (Tomiyama et al., 2002) or multiple orthogonal views (Fujiwara et al., 2004; Honkanen, 2009) with elliptical cross sections. Ríos-López et al. (2018) reconstructed a sliding droplet from orthogonal top and side views through a polynomial fit to the shadowgraphy contours under the assumption of plane symmetry. The reliance on the top view, however, introduces errors for droplets on hydrophobic substrates, due to a self-occlusion of the interface. For the 3D reconstruction from 2D images, a multitude of conventional methods have been developed, including structure from motion (Longuet-Higgins, 1981), visual hull (Laurentini, 1994), space carving (Kutulakos and Seitz, 1999), and filtered backprojection (Feldkamp et al., 1984). Fu and Liu (Fu and Liu, 2018) employed the space carving technique for the reconstruction of bubbles from contours imaged in four different viewpoints. In order to improve reconstruction accuracy, the reconstructed hull was smoothed by spline fits on multiple cross sections to emulate the effects of surface tension. Masuk et al. (2019) extended this approach by the introduction of virtual cameras, which project the reconstructed hull to novel views, in which high curvature regions were iteratively smoothed. While allowing for an accurate interface reconstruction, the aforementioned reconstruction techniques generally rely on multiple viewpoints, which can be impractical in experiments where optical access is restricted. In contrast, single-view approaches provide the benefits of easier setup and calibration, along with a more cost-effective experimental apparatus. Recent advances in deep learning reconstruction techniques offer a promising alternative for applications in which parts of the droplet dynamics are inaccessible by measurement, due to limited optical access, dynamic interfaces, complex contact lines on structured or porous surfaces, or self-occlusion. Current data-driven monocular reconstruction methods include voxel-based (Girdhar et al., 2016; Wu et al., 2016), point cloud (Fan et al., 2017; Lin et al., 2018) and mesh-based (Wang et al., 2018), and implicit representations (Chen and Zhang, 2019; Park et al., 2019; Mescheder et al., 2019; Saito et al., 2019), as well as neural rendering techniques (Niemeyer et al., 2020; Mildenhall et al., 2020). Commonly, a neural network is trained to represent a deformable 3D geometry using large paired datasets of input images and corresponding 3D shapes. The prior knowledge obtained from the training data is used to resolve ambiguities in the input data, which enables an accurate 3D reconstruction from monocular images. However, monocular shadowgraphy recordings provide only limited information about the 3D shape of gas–liquid interfaces, particularly in the depth direction, which provides little support for data-driven reconstruction techniques. Therefore, the scope of the present work is the application of a data-driven reconstruction technique based on an extended shadowgraphy with additional glare points that was previously introduced by the authors (Dreisbach et al., 2024). The basis for the volumetric reconstruction are images obtained through a purposefully developed optical measurement technique, in which color-coded glare points are used in combination with the shadowgraphy technique in order to embed additional three-dimensional information of the gas–liquid interface in the images. Subsequently, the droplet shape is reconstructed from the images by a neural network, which is trained for the physically correct reconstruction of the gas–liquid interface on numerical data. The accuracy of the proposed technique is first evaluated by the reconstruction of synthetic image data and, subsequently, the robustness of the reconstruction is investigated in experiments with increasingly deformed oscillating droplets.

2. Methodology

A neural network that was developed for the volumetric reconstruction from monocular images (Saito et al., 2019) is trained by supervised learning on a labeled dataset of droplet images and the respective
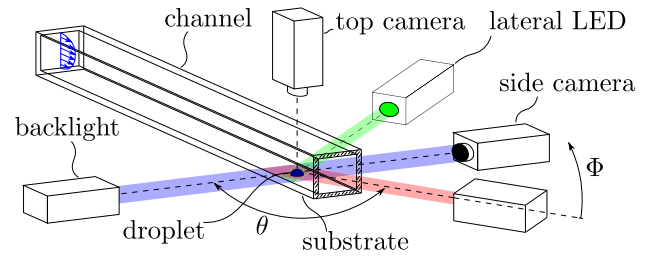

Fig. 2. Sketch of the measurement setup. Indicated are the scattering angle θ and the elevation angle Φ of the lateral light sources that determine the glare point behavior.

three-dimensional gas–liquid interface shapes. Numerical simulation provides suitable ground truth data of the gas–liquid interface that allows for the encoding of a physically correct model of the adhering droplet dynamics within the neural network. However, the numerical simulation and the images obtained in the experiments do not perfectly agree due to differences in the initial conditions, uncertainty in the experiments, and errors from modeling and numerical approximations. This matching problem between experiment and simulation is resolved by synthetic image rendering on the basis of gas–liquid interface shapes extracted from the results of the numerical simulation. In that regard, the optical setup of the experiments is reproduced accurately in a rendering environment that allows for physically correct ray tracing. Thereby, synthetic images can be generated that match the experimental recordings in visual appearance and have an exact substantive correspondence to the numerical ground truth. The neural network is trained for the physically correct reconstruction of the adhering droplet dynamics on the synthetic dataset and then employed for the reconstruction of real image data from the experiment.

In the following the fluid mechanical and optical setup of the experiments is presented in Section 2.1, which is followed by the description of the training data generation in Section 2.2. The methodology for the training of the neural network and the prediction from experimental recordings is detailed in Section 2.3 and the metrics used for the evaluation of the reconstruction performance are introduced in Section 2.4.

2.1. Experimental methods

In order to enable the volumetric reconstruction of the adhering droplet's shape, an optical measurement technique that embeds additional three-dimensional information in the images is employed. To that end, the previously introduced method by the authors (Dreisbach et al., 2023), which extends the canonical shadowgraphy technique by colored glare points from additional lateral light sources is employed.

Glare points are the bright spots visible on the gas–liquid interface of droplets and bubbles that are created when a beam of parallel light is scattered at the interface (van de Hulst and Wang, 1991). In the framework of geometrical optics, glare points occur at the exit points of any rays that are reflected or refracted on the interface at the particular scattering angle θ. As the incoming light is partly reflected and partly refracted at the interface, a portion of the light travels through the droplet and is again partly refracted and partly reflected while exiting the droplet, which repeats indefinitely. In this context, the order p of the glare point indicates the number of chords traveled through the droplet (Debye, 1908), with $p = 0$ representing externally reflected rays, $p = 1$ transmitted rays undergoing two-fold refraction at the interface, and $p \geq 2$ rays that undergo two-fold refraction and internal reflection. The position of the glare points on the projected droplet interface is dependent on the order of the glare point, the scattering angle, and the relative refractive index between the gas and liquid phases. The size of the glare points depends on the divergence angle of the incoming light and the aperture diameter of the imaging optics. Consequently,
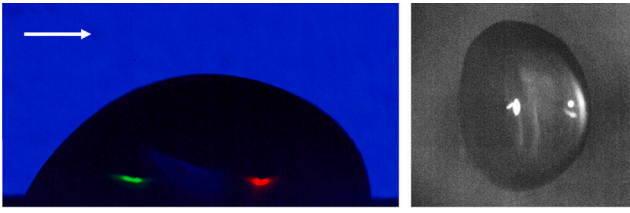
Fig. 3. Raw images recorded by the side camera (left) and the top camera (right). In both images, the main flow direction is from left to right.

Fig. 4. Ground truth gas–liquid interface extracted from numerical simulation (left) and corresponding synthetically rendered image (right).

multiple glare points of different orders can be visible simultaneously, and at certain ranges of scattering angles, certain glare points are not visible at all.

The optical setup of the glare-point shadowgraphy technique introduced in Dreisbach et al. (2023), is adapted and integrated with a flow channel that allows for the investigation of adhering droplets in external shear flows at different fluid mechanical conditions.

Within the experimental arrangement, as shown in Fig. 2, a blue LED light is used as backlight for the shadowgraphy setup, which produces an accurate projection of the droplet's contour in the image. Additionally, two lateral red and green LED light sources are mounted at specific scattering and elevation angles with respect to the droplet in order to create colored glare points on the gas–liquid interface. Three high-power *ILA_5150 LPSv3* LEDs with narrow-banded spectra and maxima in the visible spectrum at ∼455 nm (blue), ∼521 nm (green) and ∼632 nm (red) are used as illumination sources. Given the smoothness of the phase boundary, pure interface reflection ($p = 0$) can be considered for the lateral glare points. An additional glare point resulting from the two-fold refraction of the backlight during entering and exiting the gas–liquid interface ($p = 1$) appears in the center of the droplet, as can be seen in Fig. 3. As the geometric setup of the light propagation is known, additional three-dimensional information of the gas–liquid is encoded in the position and the shape of the glare points as elaborated in previous work by the authors (Dreisbach et al., 2024). The shadowgraph images of the adhering droplet with glare points are recorded by a 36-bit color dynamic range *Photron Nova R2* equipped with a *Nikon AF Micro Nikkor* 2.8/105 macro lens at 7500 frames per second (fps) and 1280 px × 512 px resolution. Moreover, a second orthogonal viewpoint from the top is recorded to obtain reference images for the evaluation of the out-of-plane accuracy of the reconstruction. For that purpose, a 12-bit monochrome dynamic range *Photron Fastcam SA4* equipped with a *Zeiss Milvus* 2/100M macro lens is used, which records at 3000 fps and 1024 px × 1024 px.

A flow channel with a 22 mm × 22 mm cross-section and 1010 mm length, made of acrylic glass (PMMA), is used in order to provide full optical access. The water droplets are placed at the downstream end of the channel, where a fully developed laminar or turbulent flow can be ensured. The volume flow rate of the air flow is measured by a *Testo* 6451 compressed air meter and adjusted by a pressure valve. In order to investigate the influence of different degrees of droplet motion, the bulk velocity of the air flow is varied in three discrete steps at $u_B = 5.85$ m/s, $u_B = 7.58$ m/s, and $u_B = 8.32$ m/s, while the droplet volume is varied between 5 and 22 µl. The corresponding Reynolds numbers, with respect to the bulk velocity and the hydraulic diameter of the channel, lie in the range of $Re_{ch} = 8500–12,100$.

The substrate on which the droplets are placed consists of PMMA, which is moderately hydrophilic with an advancing contact angle of 85° and a receding contact angle of 44°, measured by the tilting method (Maurer et al., 2016). Note that dynamic contact angles lower than 90° ensure that the top view on the contact line is never self-obstructed by the droplet's gas–liquid interface and thus a continuous tracking of the wetted area is possible. However, the low dynamic contact angles necessitate an adjustment of the lateral light sources to an elevation angle of 60° in order to ensure the occurrence of glare points on the gas–liquid interface in all frames.

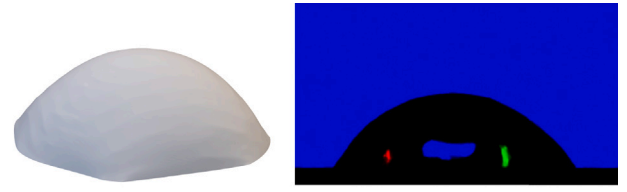## 2.2. Training dataset

The data used to train the neural network for the reconstruction of the adhering droplet's interface is obtained from numerical simulations conducted with the customized solver *hysteresisInterFoam* implemented in the open-source computational fluid dynamics (CFD) software OpenFOAM®. The solver uses the algebraic volume of fluid (VoF) method and is customized to allow for the pinning of the contact line by means of a contact angle adjustment (Krämer et al., 2021). Surface tension is modeled as a body force by the continuum surface force (CSF) model (Brackbill et al., 1992). The geometry used in the simulation model is a channel of rectangular cross-section. At the channel walls, the no-slip boundary condition and at the outlet the total pressure boundary condition is used. For the lower wall, the contact angle boundary condition is applied using the modified contact line treatment mentioned before. A block-structured grid with approximately 770,000 cells is used. Cell expansion is applied to refine the mesh close to the bottom wall. The same numerical schemes as in Krämer et al. (2021) are used in the current work. In agreement with the experiments, the simulation features a 20 µl water droplet deposited on a PMMA substrate in a fully developed turbulent channel flow at $Re_{ch} = 8500$ (Krämer et al., 2021; Burgmann et al., 2022). In order to reduce the computational requirements, the fully developed turbulent velocity profile measured in the experiments by Barwari et al. (2019) is defined at the inlet and laminar flow calculations are performed. The average numerical time step is $\Delta t \approx 1$ ms and a total of 1.1 s are simulated. The droplet is discretized by approximately 20 cells in the vertical direction and 17 cells in the streamwise and spanwise direction. The gas–liquid interface of the droplet is retrieved at each time step by extracting isosurfaces of the volume fraction at $\alpha = 0.5$.

In order to accurately simulate the glare point behavior, smooth surface meshes with a sufficiently high resolution are required. For that purpose, the resolution is increased by three consecutive iterations of mesh subdivision using linear interpolation (Dyn and Levin, 2002), followed by a smoothing of the mesh with the Taubin filter (Taubin, 1995) for 50 iterations. The quality of the smoothed meshes is assessed by plotting the mean curvature distribution over the interface and comparison to the original meshes to ensure that no additional sharp radii were introduced during mesh processing. While this smoothing procedure might affect the global shape of the droplet interface, this effect was found to be negligibly small. Furthermore, synthetic image generation by means of rendering ensures the exact correspondence of the 2D images and the 3D meshes, such that the neural network can learn to accurately reconstruct the instantaneous, physically accurate interface shape from images in the experiment.

In previous work, the authors introduced a rendering setup for the generation of synthetic images in the rendering environment *Blender* (Blender Online Community, 2018) with the *LuxCore* (Bucciarelli et al., 2018) package, which allows for physically correct ray tracing (Dreisbach et al., 2024), see also (Dreisbach, 2025, pp. 61–68). This rendering setup is adapted to accurately reproduce the optical setup of the experiments and is subsequently employed to generate synthetic glare-point shadowgraph images for each surface mesh.
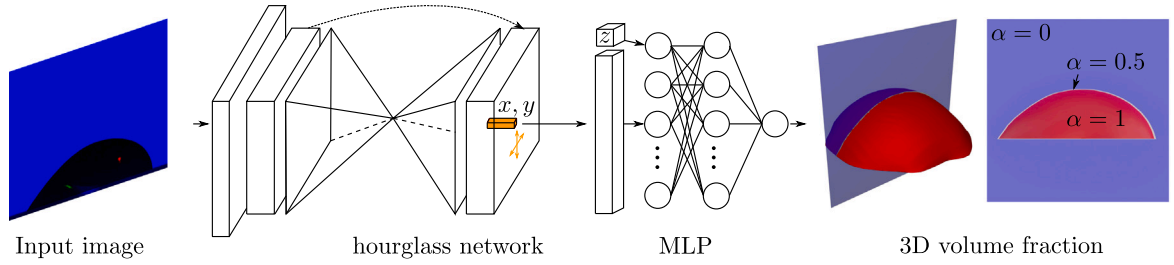
Fig. 5. Sketch of the PIFu neural network architecture. First, a convolutional hourglass network is used to extract pixel-aligned features $\mathcal{F}(x, y)$ from the input images, which are then forwarded to a second network (MLP) alongside parametric input for the depth z to predict the volume fraction in 3D space.
Source: Figure adapted from Dreisbach et al. (2024).

An example of a synthetically rendered image and the corresponding ground truth droplet shape are shown in Fig. 4. During the rendering of each time step, the droplet is rotated around the vertical axis by 360° in 10° increments in order to generate a sufficiently large training dataset, which in turn ensures the generalizability of the neural network to novel shapes. By that measure, a dataset of 1134 ground truth three-dimensional droplet shapes with respective 40,824 rendered images is obtained. The dataset is split by a ratio of 0.7/0.1/0.2 into training and separate validation and testing subsets.

2.3. Volumetric reconstruction

The Pixel-aligned Implicit Function (PIFu) neural network (Saito et al., 2019), which was developed for the volumetric reconstruction from monocular images, is trained on the synthetically rendered dataset for the physically correct reconstruction of the gas–liquid interface. The neural network learns an implicit representation of the spatio-temporal droplet geometry in the form of a level-set function. As shown in Fig. 5, the PIFu neural network consists of two consecutive modules. First, an hourglass network (Newell et al., 2016), a type of convolutional neural network (CNN), is used to extract context-rich features from the input images. Subsequently, the final feature map is sampled locally to obtain pixel-aligned features $\mathcal{F}(x, y)$ at the in-plane location x, y. Finally, a multi-layer perceptron is used to predict the scalar volume fraction α field representing the phase distribution at sampling points in 3D space (x, y, z) from the features $\mathcal{F}(x, y)$ and the additional parametric input for the depth coordinate z. Bilinear interpolation of the feature map and continuous sampling of z, along with the continuous nature of the level-set function, allow for the continuous prediction of α at any location in the 3D domain. Consequently, the reconstruction can be performed at an arbitrary resolution, independent of the training data resolution. As shown by the successful application to impinging droplets (Dreisbach et al., 2024), the encoded information in the glare points facilitates the inference of the out-of-plane component of the droplet shape. The training images are pre-processed by the superimposition of a binary mask that covers the substrate ground in the images. This introduction of prior knowledge simplifies the reconstruction task, as the differentiation between the shadowgraph contour of the droplet and the liquid–solid contact area does not need to be learned by the neural network. In order to allow for the reconstruction of different droplet volumes, the input images and the corresponding three-dimensional ground truth shapes are scaled randomly, which is a common data augmentation technique to introduce scale invariance to neural networks (Shorten and Khoshgoftaar, 2019). Since the training dataset consists of synthetic renderings of the 3D interface from various viewpoints, the trained model is agnostic to the observation angle. During the training of the network, the volume fraction at 5.000 points in 3D space is predicted simultaneously for a given input image, and the mean squared error between the predictions and the respective ground truth volume fraction is used as the objective function for the optimization of the network weights. The PIFu neural network is trained by the RMSProp optimization algorithm (Tieleman and Hinton,

2012) for eight epochs with hyperparameters according to Dreisbach et al. (2024), in particular a batch size of 12 and learning rate of 0.001, which is reduced by a factor of ten at the beginning of epochs six and eight.

The images obtained in the experiments are pre-processed prior to the reconstruction in order to further enhance the similarity to the synthetic images, which is crucial for an optimal generalization of the neural network between both image data domains (Csurka, 2017; Shrivastava et al., 2017). The mutual perturbation in the color channels of the RGB image that resulted from cross-talk in the camera sensor and the polychromatic light of the LEDs is compensated by the correction method introduced by Dreisbach et al. (2023). Thereby, the colored glare points and the shadowgraph contour are separated into the respective image channels for each light source color. In the second step, the substrate ground is masked analogously to the training data. Subsequently, each frame of the video sequence recorded by the lateral camera in the experiments is reconstructed by the neural network, in order to obtain the instantaneous three-dimensional gas–liquid interface shape at each time instance.

2.4. Evaluation metrics

The accuracy of the reconstruction is evaluated on the basis of the reconstructed volumetric droplet shapes and depending on the availability of ground truth data. The following metrics are used for evaluation:

- The three-dimensional intersection over union

$$3\text{D–IOU} = \frac{R \cap GT}{R \cup GT} \tag{1}$$

  is calculated by the fraction of the intersection volume and the union volume of the reconstructed droplet R and the ground truth GT. The 3D-IOU is an extension of the 2D-IOU (Everingham et al., 2010) to three-dimensional space, and therefore serves as a measure for the spatial volumetric accuracy of the reconstruction.
- The measured uncertainty of the reconstructed volume

$$\sigma_V = \frac{1}{\overline{V}} \sqrt{\frac{1}{n-1} \sum_{i=1}^{n} (V_{R,i} - \overline{V})^2}. \tag{2}$$

  is calculated by the standard deviation (Bendat and Piersol, 2010) of the volume of the reconstructed droplets over the course of one experiment $V_{R,i}$, normalized by the arithmetic mean $\overline{V}$ of the reconstructed volumes.

3. Results and discussion

First, the proposed reconstruction technique is evaluated on synthetic data in Section 3.1 in order to validate the capability of the method for learning the spatio-temporal dynamics of the adhering droplet and to determine the accuracy of the reconstruction. This is followed by the investigation of the reconstruction quality in the experiments at different fluid mechanical conditions and the generalization capability to different degrees of droplet deformation in Section 3.2.
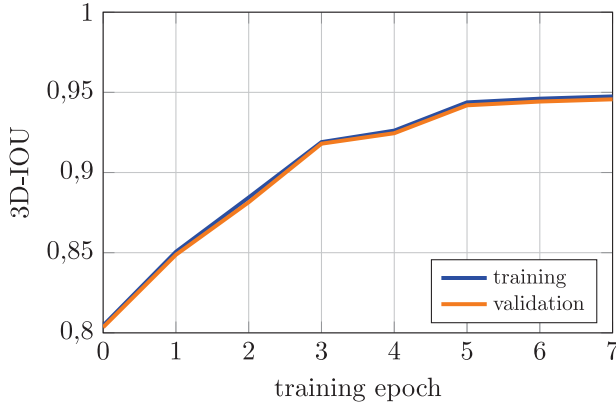
Fig. 6. Average 3D-IOU of the reconstruction on the training and validation datasets during training of the network.

3.1. Validation on synthetic image data

The accuracy of the volumetric reconstruction was tracked during the training of the neural network through the evaluation of the average 3D-IOU calculated by the arithmetic mean over 1000 samples of the training and validation dataset at every epoch. As can be seen in Fig. 6 the neural network converges to a high volumetric accuracy on both the training and the validation dataset toward the end of the training ($3D-IOU_{train} = 0.947$ and $3D-IOU_{val} = 0.946$), which is close to a perfect agreement with the ground truth ($3D-IOU_{ideal} = 1$).

The comparative analysis of all validation samples reveals that the accurate volumetric shape was reconstructed consistently throughout the dynamic deformation and oscillation of the droplet, as indicated by a low standard deviation of $\sigma_{3D-IOU} = 0.027$. The median of the volumetric accuracy on the validation dataset at the final training epoch was notably higher than the arithmetic mean ($3D-IOU_{median} = 0.954$ and $3D-IOU_{val} = 0.946$), due to outliers in the first five time steps of the validation dataset, which had a minimal accuracy of $3D-IOU_{min} = 0.793$. The shape of these outliers deviated significantly from the rest of the data distribution, thus explaining the lower reconstruction accuracy. The overall high spatial accuracy of the prediction for the validation dataset, however, implies a good generalization to unseen samples. These results indicate that the neural network successfully learned a spatio-temporal representation of the adhering droplet from the synthetic training data.

Fig. 7 shows the prediction of the phase distribution represented by the volume fraction α in three orthogonal cross-sections of the reconstructed volume. The reconstruction results for a representative sample of the validation set are shown in comparison to the ground truth shape and the respective difference of both. A volume fraction of one represents the liquid phase, whereas the gaseous phase has a volume fraction of zero, while any transitional values indicate the gas–liquid interface.

As can be seen, there is a good agreement with the ground truth in the global shape of the contour, as well as the local curvature of the reconstructed droplet shapes. However, the gas–liquid interface of the reconstruction is more diffuse than the ground truth, which is a result of the continuous implicit representation of the droplet by the neural network. In particular, the out-of-plane component of the reconstruction is more diffuse than the in-plane component, as can be seen by the comparison of Figs. 7(a) and 7(b). Furthermore, the out-of-plane component of the droplet was found to be less accurately reconstructed, which was more obvious for high error samples (see Fig. 17 in the Appendix). The more diffuse gas–liquid interface, as well as the higher deviation in the shape of the contour, indicate a higher uncertainty of the network's prediction in the out-of-plane direction. This result was expected, as fewer image features, i.e. only the glare points,
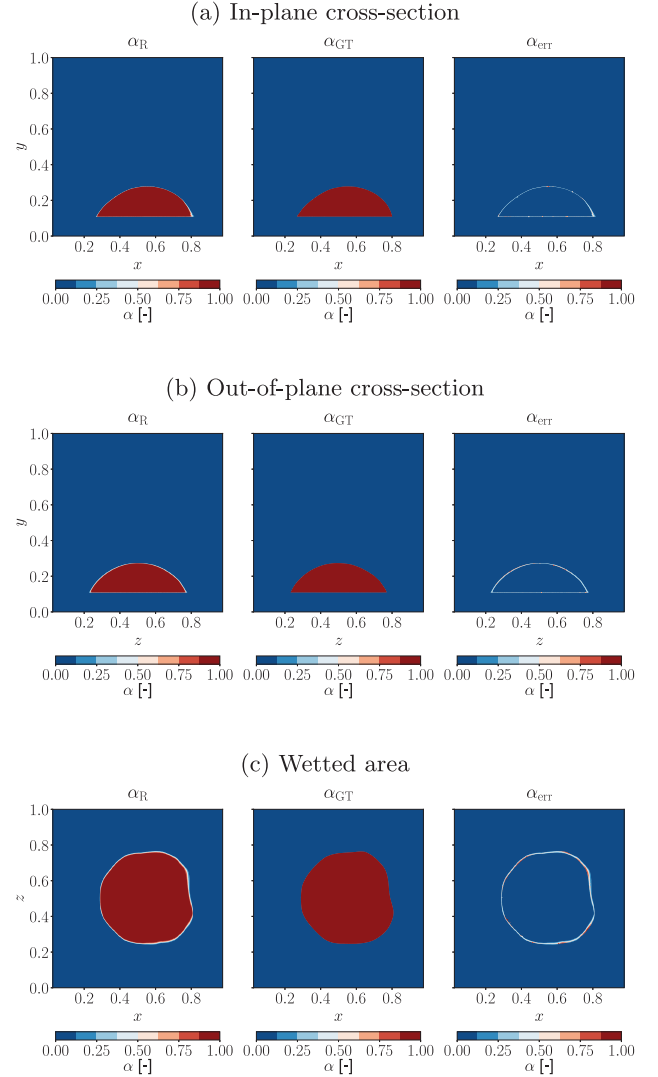

Fig. 7. Cross-sections of the volume fraction α; prediction by the neural network (left), ground truth (middle), and deviation of the prediction from the ground truth (right). In subfigures (a) and (c) the main flow direction is from left to right and in subfigure (b) the main flow direction is aligned to the image plane.

are available for the reconstruction of the out-of-plane component in comparison to the in-plane component, which has a strong basis for the reconstruction by the shadowgraph contour. Therefore, the network has to rely more on the learned knowledge from the training data for the out-of-plane reconstruction. These observations agree with the findings in previous work by the authors, in which the reconstruction of impinging droplets was considered (Dreisbach et al., 2024).

As can be seen in Fig. 7 the streamwise cross-section of the droplet is nearly planar-symmetrical, while the in-plane cross-section deviates significantly from planar symmetry due to the deformation of the droplet by the external flow. Consequently, the in-plane geometry is more difficult to reconstruct, which is alleviated by the surplus of image features available for the reconstruction. As demonstrated by the reconstruction results, both the planar symmetry of the streamwise cross-section and the deformed contour in the lateral view of the droplet are reconstructed accurately, which makes the proposed approach well-suited for the task of adhering droplet reconstruction.
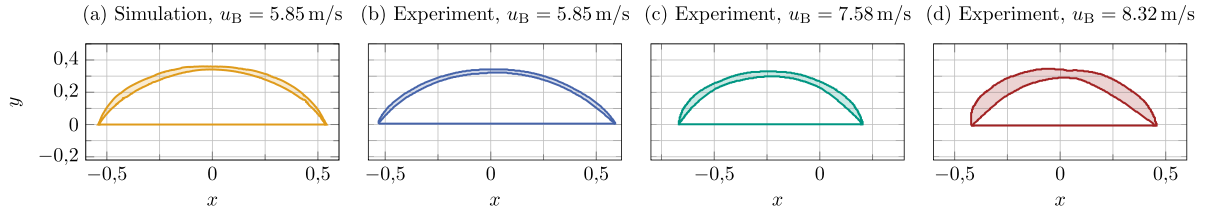
Fig. 8. Envelopes of the interface deformation for pinned oscillating droplets (cmp. Fig. 1) in the numerical simulation (left) and in the experiments (middle left to right) at different bulk velocities of external flow. Main flow direction from right to left.
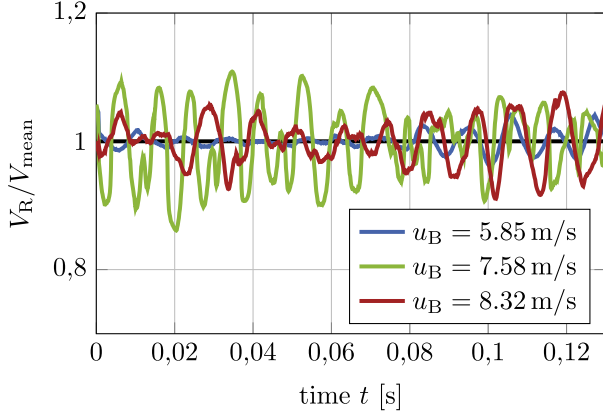
Fig. 9. Temporal evolution of the reconstructed droplet volume normalized by the mean volume for experiments with adhering droplets at different bulk velocities of external flow.

Table 1
Uncertainty σ_V of the reconstructed integral volume in percent of the mean volume for different external flow velocities averaged over all experiments conducted at a certain velocity.

Cases	$1-6$	$7-9$	$10,11$
u_B [m/s]	5.85	7.58	8.32
$\sigma_\mathrm{V}[\%\overline{V}]$	3.2	4.1	5.4

3.2. Reconstruction of experimental data

The network trained on synthetic data was applied for the volumetric reconstruction from images obtained by experiments at different external flow velocities, in particular at the measured bulk velocities of $u_\mathrm{B} = 5.85\,\mathrm{m/s}$, $u_\mathrm{B} = 7.58\,\mathrm{m/s}$ and $u_\mathrm{B} = 8.32\,\mathrm{m/s}$. Fig. 8 shows the envelopes of the droplet motion throughout the experiments for one representative case at each velocity in comparison to the numerical simulation. As can be seen, an increase in the external flow velocity resulted in a larger degree of droplet deformation. Furthermore, the comparison to the numerical data reveals that only at $u_\mathrm{B} = 5.85\,\mathrm{m/s}$ a similar degree of deformation can be observed in the experiments. Consequently, the neural network trained on the numerical data has to generalize to significantly more deformed and unknown droplet shapes in order to successfully reconstruct the experiments at $u_\mathrm{B} = 7.58\,\mathrm{m/s}$ and $u_\mathrm{B} = 8.32\,\mathrm{m/s}$. Note, that the same representative experiments (cases 1, 8, and 10) will be the subject of the following evaluation unless stated otherwise. The results of further experiments can be found in the Appendix.

As no volumetric ground truth data is available for the reconstruction from images recorded in the experiments, the temporal evolution of the reconstructed droplet volume is considered for the evaluation of the reconstruction accuracy. In the experiments, no significant evaporation occurred within the time frame of one recorded image series (1000 images over 133.3 ms) and, consequently, the volume of the droplet can be assumed to be constant.
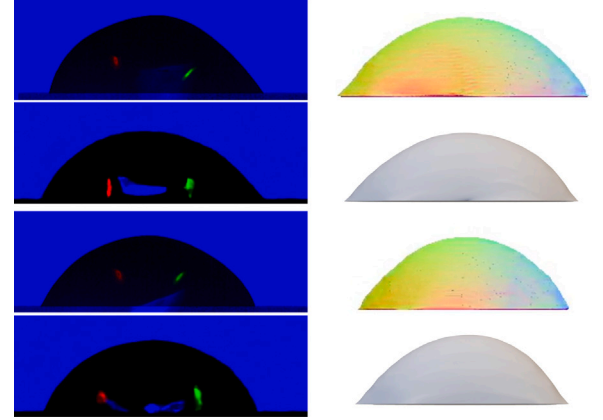

Fig. 10. Input images (left) and out-of-plane projection (right) of the respective three-dimensional interfaces for the reconstruction at $u_\mathrm{B} = 8.32\,\mathrm{m/s}$. Rows one and three show the experimental recordings and the corresponding reconstructed interfaces and rows two and four show matching samples from the synthetic training dataset.

Fig. 9 shows the temporal evolution of the normalized integral volume of the reconstructed droplet for one representative experiment at each evaluated velocity of the external flow. As can be seen, the volume of the reconstruction fluctuates periodically around the mean, with an increasing amplitude toward higher velocities of the external flow, i.e. higher degrees of droplet deformation. The measured uncertainties of the reconstruction, as detailed in Table 1, further underline that the reconstruction at higher degrees of droplet deformation is subject to higher uncertainty. As indicated by the low uncertainty for the reconstruction at $u_\mathrm{B} = 5.85\,\mathrm{m/s}$ the neural network trained on synthetic image data generalizes well to the reconstruction of experiments with a similar degree of droplet deformation to the numerical simulation that underlies the training data. The successful reconstruction of the significantly more deformed gas–liquid interface in the experiments at $u_\mathrm{B} = 7.58\,\mathrm{m/s}$ and $u_\mathrm{B} = 8.32\,\mathrm{m/s}$, which resulted in droplet shapes unknown to the neural network, indicates the trained network can extrapolate to different fluid mechanical conditions. Furthermore, these results demonstrate the robustness of the method, which, however, is constrained by a reduced accuracy for the reconstruction of different data.

The periodical oscillation of the reconstructed volume was found to coincide with the oscillation of the droplet contour. Moreover, the input images to the volumetric reconstruction at the extrema of the volumetric deviation appear similar. Fig. 10 shows examples of the input images from the experiment that resulted in a local maximum (first row) and minimum (third row) of the volume and the respective out-of-plane projection of the reconstructed droplet shape. In particular, the position of the glare points relative to each other and to the contour of the droplet was similar between the groups of input images that resulted in either the maxima or minima of reconstructed volume, which indicates a similar shape of the droplet interface. Most saliently, a low position of the blue $p = 1$ glare point in the input images resulted
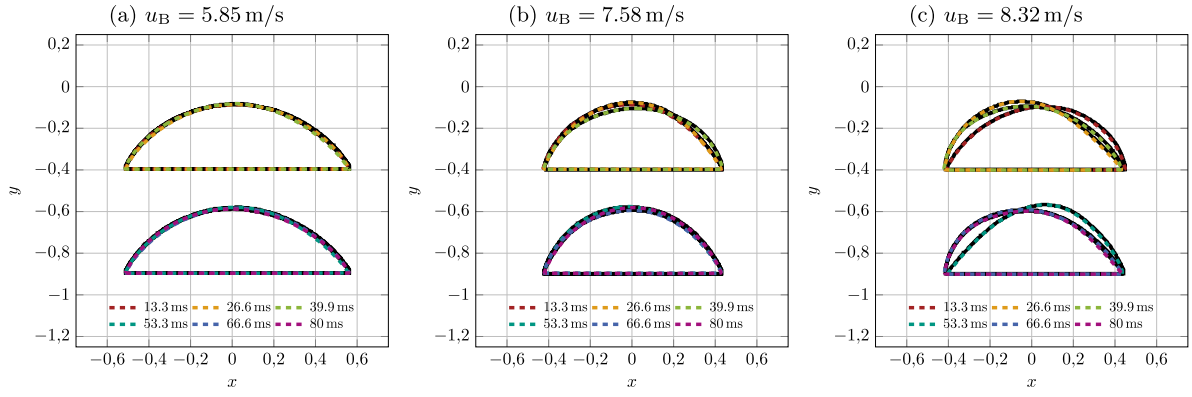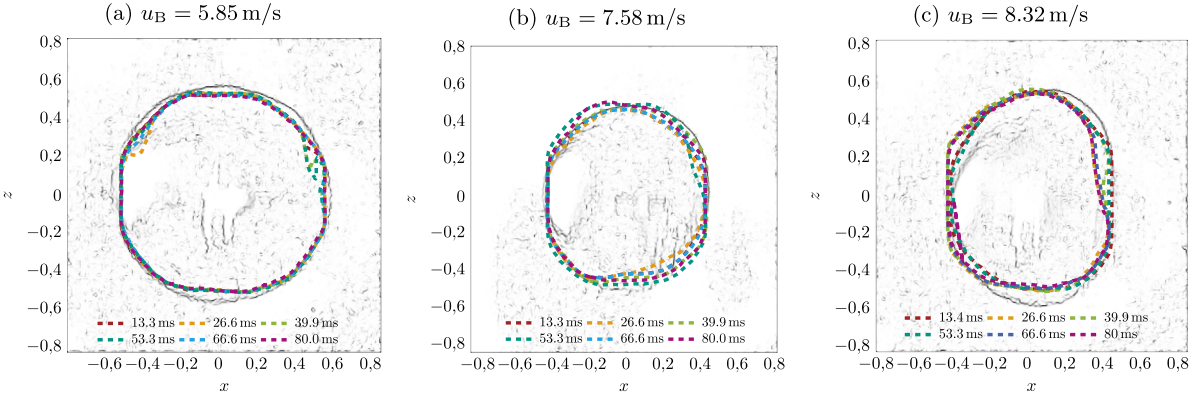
Fig. 11. Temporal evolution of the reconstructed in-plane contour for different bulk velocities of external flow. The dashed colored lines indicate the reconstructed contours at different times and the black solid lines indicate the corresponding contours observed in the experiments. The main flow direction is from right to left.
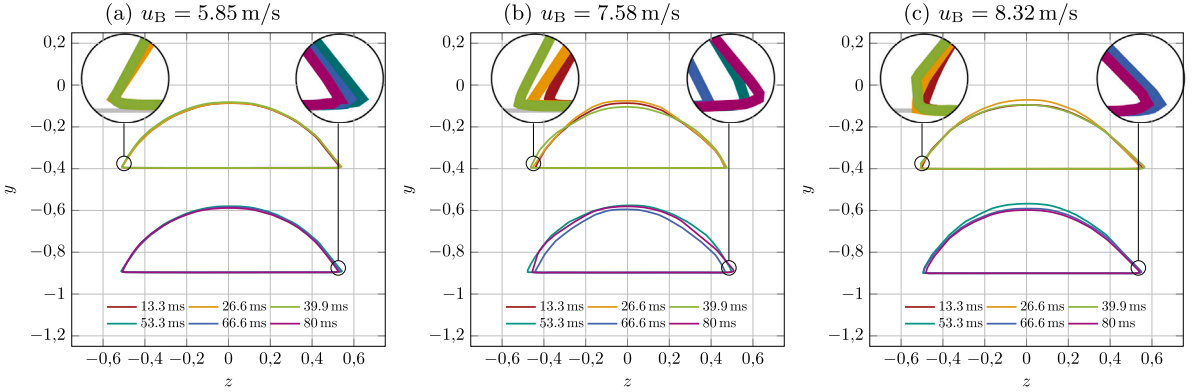
Fig. 12. Temporal evolution of the reconstructed out-of-plane contour for different bulk velocities of external flow. The solid colored lines indicate the reconstructed contours at different times. The image plane is aligned with the main flow direction.

Fig. 13. Temporal evolution of the reconstructed wetted area for different bulk velocities of external flow. The dashed colored lines indicate the reconstructed contours at different times and the grayscale image in the background indicates the corresponding contour observed in the experiments. The main flow direction is from right to left.

in a minimum volume, while a maximum in the reconstructed volume correlated with a high position of the $p = 1$ glare point.

For both cases, synthetic images with similar relative glare point positions can be found in the training dataset, which are shown in rows two and four in Fig. 10. Note, that Fig. 10 shows sample images from the experiments at $u_B = 8.32$ m/s for better visibility of the differences between the minimum and maximum case, as this experiment resulted in the highest deviations in the reconstructed volume. Consequently, the contour of the droplet in the reconstruction is more deformed than the synthetic training data. However, the reconstruction at lower velocities follows the same behavior. The comparison of the out-of-plane projection between the reconstruction and the training data

reveals a very similar shape of the contour. These results indicate that the neural network successfully learned the relation of the glare point positions to the three-dimensional geometry of the droplet and that this encoding of 3D information can be applied for depth estimation during reconstruction. However, as the neural network has been trained for the reconstruction of different droplet volumes by an augmentation of the training data, as described in Section 2.3, it is agnostic to the volume of the droplet. Consequently, the shape of the contour is reconstructed with disregard to the integral volume of the droplet and thus the volume of the reconstruction is not conserved in time.

In order to evaluate the in-plane and the out-of-plane accuracy of the reconstruction in more detail, two orthogonal projections of the

reconstructed droplet interface are compared to the side- and top-view contours extracted from the corresponding images recorded in the experiments. The results of the in-plane reconstruction for different external flow velocities are presented in Fig. 11 and the results of the out-of-plane reconstruction are shown in Fig. 12. As can be seen, there is an almost identical agreement of the reconstructed in-plane contours with the respective contours from the experiment, which underlines the findings of a high in-plane accuracy for the reconstruction of synthetic data. The planar symmetry in the out-of-plane direction, which was expected due to the symmetry of the flow, was also reconstructed well for the experimental data. However, the reconstruction exhibits a fluctuation in the out-of-plane direction that is particularly noticeable in Fig. 12(b). This out-of-plane fluctuation is identified as the sole cause for the uncertainty of the volumetric reconstruction since the in-plane reconstruction is highly accurate. The out-of-plane reconstruction relies on the learned droplet geometry and the encoding of three-dimensional information by the glare points and, therefore, the accuracy of the reconstruction is reduced the more the input data deviates from the training data distribution. The in-plane reconstruction is based on the image features, most importantly the contour of the shadowgraph, which provides a significantly larger amount and more direct information for the reconstruction. As the in-plane reconstruction adheres closely to the contour in the images, the neural network adapts well to unknown shapes outside of the training data distribution. These results fall in line with the observed uncertainty of the out-of-plane reconstruction for synthetic data in Section 3.1 and previous observations of impinging droplets (Dreisbach et al., 2024).

The accuracy of the depth estimation is further evaluated by the comparison of the top-view projection of the reconstruction to the footprint of the droplet observed in the experiments through the top-view camera. As can be seen in Fig. 8, the contact line of the droplet stays pinned during the duration of the experiments and the wetted area is therefore constant over time. Fig. 13 shows the contour of the contact lines extracted from the experimental recordings at different external flow velocities. The contours from the experiments are overlayed with the projected contours of the reconstructed droplet shapes for six different time instances. As can be seen, the shape of the wetted area in the reconstruction is similar to the experiment and self-similar over time for $u_B = 5.85\,\text{m/s}$, while there is a larger deviation to the ground truth at higher external flow velocities. The aspect ratio of the footprint changes significantly toward higher velocities as the droplet is deformed by the external flow. Remarkably, the neural network successfully reconstructs these different aspect ratios, which is a significant extrapolation from the training data, which only contained one simulated case at the external flow velocity $u_B = 5.85\,\text{m/s}$, for which the footprint had an aspect ratio close to one. For the same velocity in the experiments ($u_B = 5.85\,\text{m/s}$) a very good agreement of the reconstruction with the ground truth was reached. At higher velocities ($u_B = 7.58$ and $u_B = 8.32$) the out-of-plane extent of the droplet was generally underestimated and reconstructed with a higher uncertainty, as indicated by the larger variation in the reconstructed footprints. Furthermore, the unknown droplet shapes in the experiments related to higher aspect ratios of the wetted area were reconstructed close to the distribution of shapes in the training data, thus revealing a bias of the trained model. Consequently, the reconstruction exhibits increasing errors the more the real gas–liquid interface shape deviates from the training data distribution. For all velocities, the contour of the reconstruction is more angular in comparison to the experiment, but similar to the training data, as seen in Fig. 7, which is a further indication of model bias. However, these results also demonstrate that the geometry of the droplet was learned faithfully to the training dataset by the network. Therefore, the accuracy of the reconstruction is dependent on the truthful representation of the droplet dynamics in the training data. The successful reconstruction of unknown droplet shapes with higher aspect ratios indicates that the network learned to utilize the glare points for the depth estimation. These results indicate

Table 2
Average time required for the reconstruction of one time step at different output resolutions.

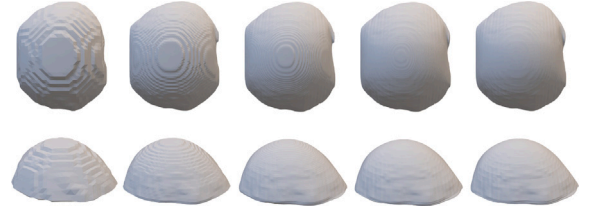| Grid nodes	64^3	128^3	256^3	512^3	$1,024^3$
Time [s]	0.2	2.5	4.4	17.0	266.5

Fig. 14. Volumetric reconstruction at different resolution for the same input image from the experiment at $u_B = 8.32\,\text{m/s}$, from left to right: 64^3, 128^3, 256^3, 512^3, 1024^3 grid nodes resolution.

that the prior knowledge obtained from the numerical training data induces a bias of the trained droplet model toward the reconstruction of geometries close to the training data distribution in the out-of-plane direction. This bias reduces the accuracy, the further the test data deviates from the training data distribution. However, it was also found to facilitate a robust reconstruction, as the bias encourages the reconstruction of plausible shapes, which prevents a breakdown of the prediction for unknown input data. Consequently, the error increases slowly for predictions outside of the training data distribution. Therefore, retraining the network on specific training data that considers the expected distribution of the 3D gas–liquid interface shapes in the experiments is expected to yield the most accurate reconstruction results. It was found that a moderate amount of data (one CFD simulation) is sufficient to train the network, while a greater variance and size of the dataset did not yield significant improvement. These results suggest that a more specific, though smaller, dataset is optimal for training the proposed network.

3.3. Surface quality of the reconstructed interfaces

The implicit representation of the three-dimensional droplet geometry by the PIFu neural network (Saito et al., 2019) allows for the reconstruction at an arbitrary resolution. As higher resolutions are expected to result in a higher quality of the surface, but also increased computational costs, in the following the results of the reconstruction at different resolutions were evaluated. Table 2 details the average time required for the reconstruction of one time step at different resolutions. The domain for the reconstruction was discretized by an equidistant 3D grid with the same amount of grid nodes in all directions. The trained PIFu network was sampled on this grid to predict the scalar volume fraction field of the phase distribution. Subsequently, the isosurface extraction algorithm marching cubes (Lewiner et al., 2003; Lorensen and Cline, 1987) was employed to reconstruct the surface mesh from the volume fraction field. All calculations were performed on a single Nvidia RTX A5000 graphics processing unit. As expected, the computational costs grow quickly toward higher resolutions. However, the octree (Meagher, 1982) structure used during reconstruction significantly reduces the reconstruction time at higher resolutions up to 512^3 grid nodes, which becomes obvious by the deviation from the cubic growth rule that would be expected otherwise. Note that this trend only holds true until 512^3 grid nodes due to given hardware limitations.

Fig. 14 shows the results of the volumetric reconstruction at different resolutions for the same input image obtained in the experiments at an external flow velocity $u_B = 8.32\,\text{m/s}$. As can be seen, there is a significant visual improvement in the surface smoothness as the resolution increases from 64^3 to 512^3. However, with the increase
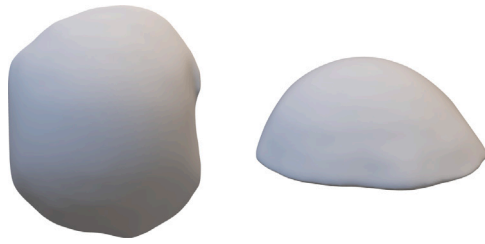
Fig. 15. Smoothed volumetric reconstruction at 512^3 grid nodes resolution.

in the resolution from 512^3 to $1,024^3$ grid nodes, the quality of the reconstruction did not increase further. In fact, a marginal decrease of the surface quality can be observed, as small-scale ripples appear on the surface for a resolution of $1,024^3$ nodes, which are likely smoothed out by lower resolutions. Considering the total time of 4.7 h required for the reconstruction of one experiment with 1000 frames, a resolution of 512^3 grid nodes was found to be optimal within the scope of obtaining accurate and smooth surface meshes for distortion correction. Note, that all reconstruction results presented in this work have a resolution of 512^3 grid nodes.

It should be noted, that the presented reconstruction method is able to reconstruct the gas–liquid interface of the droplet at a significantly higher resolution compared to the training data. The spatial resolution of the numerical simulation that underlies the training data was 20 cells in the vertical direction and 17 cells in the streamwise and spanwise direction at $t = 0$. These results demonstrate that the neural network has the capability to learn a highly accurate representation of the droplet geometry even from data much coarser than the targeted reconstruction resolution. Furthermore, the approach of smoothing the ground truth gas–liquid interfaces that were extracted from the numerical simulation is validated by the positive reconstruction results. In order to further enhance the surface quality of the reconstruction, smoothing by means of the Taubin filter (see Section 2.2) is employed.

As shown in Fig. 15, the proposed process yields a smooth surface mesh of the droplet's gas–liquid interface that can be used for the intended distortion correction of PIV measurements. Such distortion correction techniques require surface meshes that exhibit both a high fidelity to the true interface shape in the experiments and a smooth curvature, in order to allow for the accurate calculation of light refraction at the gas–liquid interface. The prediction of the scalar volume fraction field for the phase distribution by the PIFu neural network serves as an accurate basis for the surface reconstruction. In this study, the efficient implementation (Lewiner et al., 2003) of the marching cubes algorithm (Lorensen and Cline, 1987) is employed to reconstruct the surface meshes. However, alternative isosurface extraction algorithms, including extensions of the marching cubes algorithm (Westermann et al., 1999; Kobbelt et al., 2001), methods based on Delaunay triangulation (Boissonnat and Oudot, 2005), or methods used in the numerical simulation of two-phase flows, such as the Piecewise-Linear Interface Calculation (PLIC) scheme (Youngs, 1982), may offer improved reconstruction performance. Therefore, further research is required to assess the suitability of the reconstructed surfaces for distortion correction in the experiments. This includes further development of surface reconstruction methods and smoothing operations, as well as experimentally validating the reconstructed meshes in the ray tracing approach to confirm their feasibility for distortion correction.

4. Conclusion

The proposed method allows for the accurate reconstruction of the gas–liquid interface of adhering droplets in external shear flows from images recorded by means of a purposefully developed, yet simple optical measurement setup. The evaluation using synthetic image data reveals that a high spatial accuracy can be reached by training the PIFu neural network on a synthetically rendered dataset based on numerical simulation. Furthermore, the positive results for the reconstruction based on images recorded in the experiments demonstrate the applicability of the neural network trained on synthetic data to the real-world use case and thus validate the approach of training on synthetic data.

In particular, the in-plane component of the reconstruction reaches an almost identical agreement to the ground truth, as the contour of the shadowgraph presents a strong basis for the in-plane reconstruction. The out-of-plane reconstruction relies on the learned droplet geometry, in addition to the three-dimensional information encoded in the glare points, which is more sparsely distributed across the droplet interface. Consequently, the uncertainty of the reconstruction is higher in the out-of-plane direction. The successful reconstruction of adhering droplets at much higher flow velocities and greater deformation than in the training data shows that the method can effectively handle and predict new, unknown shapes. It can be concluded that the combination of the learned geometry and the depth encoding by the glare points results in a robust and flexible model of the gas–liquid interface dynamics that can be used for the extrapolation to different flow conditions outside of the training data distribution. The proposed method leverages the planar symmetry of the setup, simplifying the depth prediction along the streamwise direction. Concurrently, the more significant deformation of the droplet in spanwise direction is imaged directly via the shadowgraph contour, thus reserving the previously mentioned high in-plane accuracy for the direction that undergoes more significant deformation.

The implicit representation of the interface by the neural network allows for the reconstruction at a fine resolution, while the training on the results of numerical simulation facilitates a high fidelity of the reconstructed contours to the underlying physics. Therefore, the reconstructed gas–liquid interfaces are both spatially accurate and smooth, which makes the proposed method well-suited for distortion correction of PIV images, as the accurate reconstruction of the local curvature of the interface is important for the correct calculation of the refraction that causes the distorted velocity fields. In comparison to the current state-of-the-art approach for distortion correction, in which rotational symmetry of the gas–liquid interface is assumed, the presented approach becomes increasingly beneficial toward higher external flow velocities that result in larger degrees of droplet deformation and thus non-axis-symmetrical droplet shapes.

While the reconstruction at greater velocities of external flow beyond the training data proved successful, a higher reconstruction accuracy could be reached by re-training the neural network with more appropriate data, which represents the expected distribution of deformed interface shapes. Furthermore, the bias of the network toward certain geometries can most likely be reduced by a greater variation ground truth shapes in the training dataset. Thereby, the flexibility and robustness of the trained model could be further enhanced. Further improvements in the reconstruction accuracy can be expected from an increased resolution of the numerical simulation that is used to source the training data. The effect is two-fold, on the one hand, more accurate three-dimensional ground truth data facilitates the learning of the droplet geometry, and on the other hand, more finely resolved surface meshes would increase the quality of the synthetic images rendered by ray tracing. In future work, the introduction of physical constraints – such as mass or momentum conservation – into the training process via physics-informed neural networks (Raissi et al., 2019) could be used to further increase the accuracy of the reconstruction. While presented alongside results for hydrophilic substrates, the proposed method can be straightforwardly applied to hydrophobic substrates, as the monocular side view input remains unobstructed for contact angles greater than 90 degrees (Dreisbach et al., 2024).
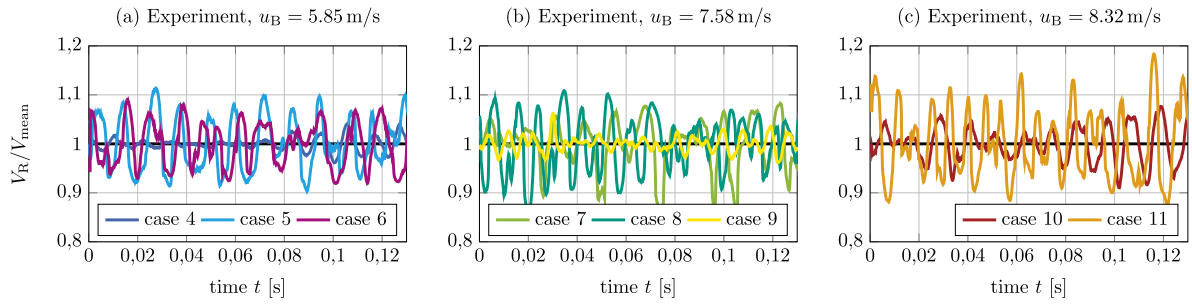
Fig. 16. Temporal evolution of the normalized integral volume of the reconstruction for adhering droplets in external shear flows at different bulk velocities $u_B = 5.85\,\text{m/s}$, $u_B = 7.58\,\text{m/s}$, and $u_B = 8.32\,\text{m/s}$.

CRediT authorship contribution statement

Maximilian Dreisbach: Writing – original draft, Visualization, Validation, Software, Methodology, Investigation, Formal analysis, Data curation, Conceptualization. **Itzel Hinojos:** Writing – review & editing, Data curation. **Jochen Kriegseis:** Writing – review & editing, Resources, Project administration. **Alexander Stroh:** Writing – review & editing, Resources, Project administration, Conceptualization. **Sebastian Burgmann:** Writing – review & editing, Supervision, Conceptualization.

Declaration of competing interest

The authors declare that they have no known competing financial interests or personal relationships that could have appeared to influence the work reported in this paper.

Acknowledgments

Appendix

The temporal evolution of the normalized integral volume of the reconstructed droplet is presented in Fig. 9 for one representative experiment at each evaluated velocity u_B of the external flow. These results are further detailed in Fig. 16, showing the evolution of the reconstructed droplet volume for all cases at the respective velocities $u_B = 5.85\,\text{m/s}$, $u_B = 7.58\,\text{m/s}$, and $u_B = 8.32\,\text{m/s}$. Fig. 17 shows the reconstructed phase distribution represented by the volume fraction α in comparison to the ground truth data in three orthogonal cross-sections for one example of the validation data with high errors. As can be seen, the out-of-plane reconstruction exhibits significantly larger errors in comparison to the in-plane reconstruction, which falls in line with the observations of the error distribution for a low error sample in Fig. 7.

Data availability

All data that support the findings of this study, including the weights of the trained neural networks and any supplementary files are uploaded to KITopen.
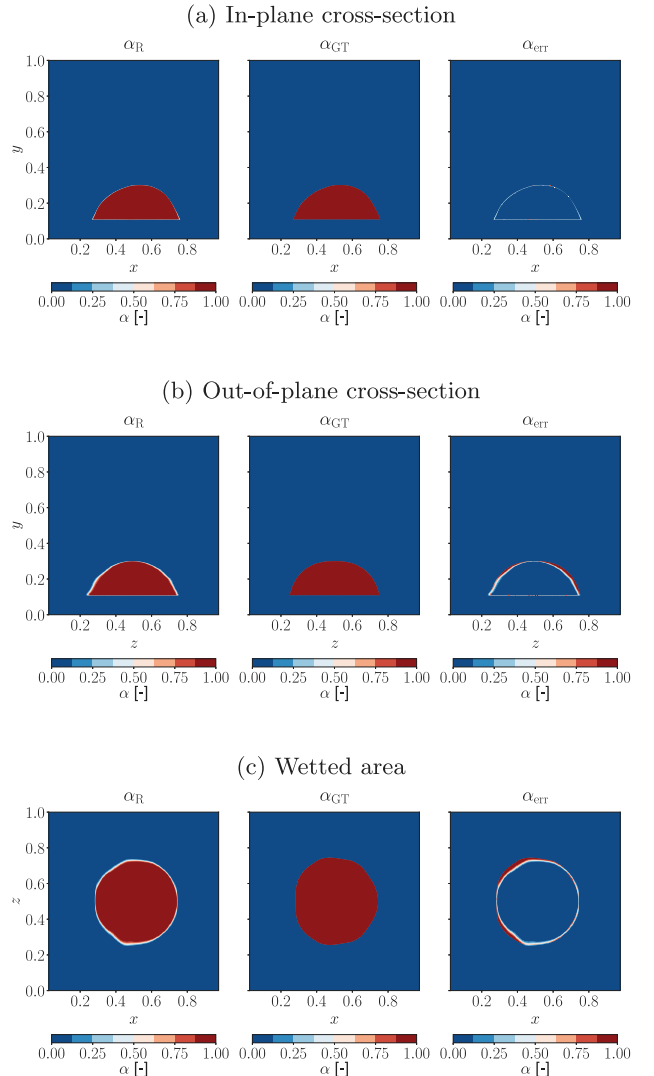
Fig. 17. Cross-sections of the volume fraction α; prediction by the neural network (left), ground truth (middle), and deviation of the prediction from the ground truth (right). In subfigures (a) and (c) the main flow direction is from left to right and in subfigure (b) the main flow direction is aligned to the image plane.

References

Barwari, B., Burgmann, S., Bechtold, A., Rohde, M., Janoske, U., 2019. Experimental study of the onset of downstream motion of adhering droplets in turbulent shear flows. Exp. Therm. Fluid Sci. 109, 109843.

Barwari, B., Burgmann, S., Janoske, U., 2018. Deformation and movement of adhering droplets in shear flow. In: 5th International Conference on Experimental Fluid Mechanics, Munich, July 2-4.

Bendat, J.S., Piersol, A.G., 2010. Random data : analysis and measurement procedures, 4th ed. In: Wiley series in probability and statistics, Wiley, (Online-Ausg.).

Bilsing, C., Janoske, U., Czarske, J., Büttner, L., Burgmann, S., 2025. 3D-3C measurements of flow reversal in small sessile drops in shear flow. Int. J. Multiph. Flow 182, 105017.

Bilsing, C., Nützenadel, E., Burgmann, S., Czarske, J., Büttner, L., 2024. Adaptive-optical 3D microscopy for microfluidic multiphase flows. Light.: Adv. Manuf. 5, 1.

Blender Online Community, 2018. Blender - A 3D Modelling and Rendering Package. Blender Foundation, Stichting Blender Foundation.

Boissonnat, J.-D., Oudot, S., 2005. Provably good sampling and meshing of surfaces. Graph. Model. 67 (5), 405–451.

Brackbill, J., Kothe, D., Zemach, C., 1992. A continuum method for modeling surface tension. J. Comput. Phys. 100 (2), 335–354.

Bucciarelli, D., Wendsche, S., Klemm, M., Sandbacka, P., Ehoumanand, C., Castagnini, A., Quade, G., Ghotbi, O., 2018. Luxcorerender project. LuxCoreRender Project.

Burgmann, S., Barwari, B., Janoske, U., 2018a. Inner flow structure of an adhering oscillating droplet in shear flow. In: 19th Int. Symp. on the Application of Laser and Imaging Techniques to Fluid Mechanics, Lissabon, July 16-19.

Burgmann, S., Barwari, B., Janoske, U., 2018b. Oscillation of adhering droplets in shear flow. In: 5th International Conference on Experimental Fluid Mechanics, Munich, July 2-4.

Burgmann, S., Blank, M., Panchenko, U., Wartmann, J., 2013. μPIV measurements of two-phase flows of an operated direct methanol fuel cell. Exp. Fluids 54.

Burgmann, S., Dues, M., Barwari, B., Steinbock, J., Büttner, L., Czarske, J., Janoske, U., 2021. Flow measurements in the wake of an adhering and oscillating droplet using laser-Doppler velocity profile sensor. Exp. Fluids 62 (3), 47.

Burgmann, S., Krämer, V., Rohde, M., Dues, M., Janoske, U., 2022. Inner and outer flow of an adhering droplet in shear flow. Int. J. Multiph. Flow 153, 104140.

Carre, A., Shanahan, M.E.R., 1995. Drop motion on an inclined plane and evaluation of hydrophobia treatments to glass. J. Adhes. 49 (3–4), 177–185.

Chen, Z., Zhang, H., 2019. Learning implicit fields for generative shape modeling. In: 2019 IEEE/CVF Conference on Computer Vision and Pattern Recognition (CVPR). IEEE, pp. 5932–5941.

Csurka, G., 2017. Domain adaptation in computer vision applications. Springer International Publishing, Cham.

van de Hulst, H.C., Wang, R.T., 1991. Glare points. Appl. Opt. 30 (33), 4755–4763.

Debye, P., 1908. Das elektromagnetische Feld um einen Zylinder und die Theorie des Regenbogens. Phys. Z 9 (1464), 775–778.

Dreisbach, M., 2025. Spatio-Temporal Interface Reconstruction by Means of Glare Points and Deep Learning (Ph.D. thesis). Karlsruhe Institute of Technology.

Dreisbach, M., Blessing, S., Brunn, A., Michaux, F., Stroh, A., Kriegseis, J., 2023. Three-dimensional encoding of a gas–liquid interface by means of color-coded glare points. Exp. Fluids 64 (3), 53.

Dreisbach, M., Kriegseis, J., Stroh, A., 2024. Spatio-temporal reconstruction of droplet impingement dynamics by means of color-coded glare points and deep learning. Meas. Sci. Technol. 36 (1), 015304.

Dussan, V.E.B., 1987. On the ability of drops to stick to surfaces of solids. Part 3. The influences of the motion of the surrounding fluid on dislodging drops. J. Fluid Mech. 174, 381–397.

Duxenneuner, M.R., Fischer, P., Windhab, E.J., Cooper-White, J.J., 2014. Simultaneous visualization of the flow inside and around droplets generated in microchannels. Microfluid. Nanofluidics 16 (4), 743–755.

Duxenneuner, M., Pust, O., Fischer, P., Windhab, E., Cooper-White, J., 2009. Flow visualization of a forming droplet in a micro channel with FlexPIV. In: 8th International Symposium on Particle Image Velocimetry, PIV'09 : August 25 - 28, 2009, Melbourne, Australia.

Dyn, N., Levin, D., 2002. Subdivision schemes in geometric modelling. Acta Numer. 11, 73–144.

ElSherbini, A., Jacobi, A., 2004. Liquid drops on vertical and inclined surfaces. J. Colloid Interface Sci. 273 (2), 556–565.

Esposito, A., Montello, A.D., Guezennec, Y.G., Pianese, C., 2010. Experimental investigation of water droplet–air flow interaction in a non-reacting PEM fuel cell channel. J. Power Sources 195 (9), 2691–2699.

Everingham, M., Van Gool, L., Williams, C.K.I., Winn, J., Zisserman, A., 2010. The pascal visual object classes (VOC) challenge. Int. J. Comput. Vis. 88 (2), 303–338. http://dx.doi.org/10.1007/s11263-009-0275-4.

Extrand, C.W., Kumagai, Y., 1995. Liquid drops on an inclined plane: The relation between contact angles, drop shape, and retentive force. J. Colloid Interface Sci. 170 (2), 515–521.

Fan, H., Su, H., Guibas, L., 2017. A point set generation network for 3D object reconstruction from a single image. In: 2017 IEEE Conference on Computer Vision and Pattern Recognition (CVPR). IEEE, pp. 2463–2471.

Fan, J., Wilson, M., Kapur, N., 2011. Displacement of liquid droplets on a surface by a shearing air flow. J. Colloid Interface Sci. 356 (1), 286–292.

Feldkamp, L.A., Davis, L.C., Kress, J.W., 1984. Practical cone-beam algorithm. J. Opt. Soc. Am. A 1 (6), 612.

Fu, S.C., Leung, W.T., Chao, C.Y.H., 2014. Detachment of droplets in a fully developed turbulent channel flow. Aerosol Sci. Technol. 48 (9), 916–923.

Fu, Y., Liu, Y., 2018. 3D bubble reconstruction using multiple cameras and space carving method. Meas. Sci. Technol. 29 (7), 075206.

Fujiwara, A., Danmoto, Y., Hishida, K., Maeda, M., 2004. Bubble deformation and flow structure measured by double shadow images and PIV/LIF. Exp. Fluids 36 (1), 157–165.

Furmidge, C., 1962. Studies at phase interfaces. I. The sliding of liquid drops on solid surfaces and a theory for spray retention. J. Colloid Sci. 17 (4), 309–324.

Girdhar, R., Fouhey, D.F., Rodriguez, M., Gupta, A., 2016. Learning a predictable and generative vector representation for objects. In: Leibe, B., Matas, J., Sebe, N., Welling, M. (Eds.), Computer Vision – ECCV 2016. Springer International Publishing, Cham, pp. 484–499.

Gupta, A.K., Basu, S., 2008. Deformation of an oil droplet on a solid substrate in simple shear flow. Chem. Eng. Sci. 63 (22), 5496–5502.

Higashine, M., Katoh, K., Wakimoto, T., Azuma, T., 2008. Profiles of liquid droplets on solid plates in gravitational and centrifugal fields. J. Jpn. Soc. Exp. Mech. 8, 49–54.

Honkanen, M., 2009. Reconstruction of a three-dimensional bubble surface from high-speed orthogonal imaging of dilute bubbly flow. In: Mammoli, A.A., Brebbia, C.A. (Eds.), Computational Methods in Multiphase Flow V. In: WIT Transactions on Engineering Sciences, WIT Press Southampton, UK, pp. 469–480.

Kandlikar, S.G., Steinke, M.E., 2002. Contact angles and interface behavior during rapid evaporation of liquid on a heated surface. Int. J. Heat Mass Transf. 45 (18), 3771–3780.

Kang, K.H., Lee, S.J., Lee, C.M., Kang, I.S., 2004. Quantitative visualization of flow inside an evaporating droplet using the ray tracing method. Meas. Sci. Technol. 15 (6), 1104.

Karlsson, L., Lycksam, H., Ljung, A.-L., Gren, P., Lundström, T.S., 2019. Experimental study of the internal flow in freezing water droplets on a cold surface. Exp. Fluids 60 (12), 182.

Kinoshita, H., Kaneda, S., Fujii, T., Oshima, M., 2007. Three-dimensional measurement and visualization of internal flow of a moving droplet using confocal micro-PIV. Lab A Chip 7 (3), 338–346.

Kobbelt, L.P., Botsch, M., Schwanecke, U., Seidel, H.-P., 2001. Feature sensitive surface extraction from volume data. In: Proceedings of the 28th Annual Conference on Computer Graphics and Interactive Techniques. ACM, pp. 57–66.

Korte, C., Jacobi, A.M., 2001. Condensate retention effects on the performance of plain-fin-and-tube heat exchangers: Retention data and modeling. J. Heat Transf. 123 (5), 926–936.

Krämer, V., Barwari, B., Burgmann, S., Rohde, M., Rentschler, S., Holzknecht, C., Gmelin, C., Janoske, U., 2021. Numerical analysis of an adhering droplet applying an adapted feedback deceleration technique. Int. J. Multiph. Flow 145, 103808.

Kumbur, E.C., Sharp, K.V., Mench, M.M., 2006. Liquid droplet behavior and instability in a polymer electrolyte fuel cell flow channel. J. Power Sources 161 (1), 333–345.

Kutulakos, K., Seitz, S., 1999. A theory of shape by space carving. In: Proceedings of the Seventh IEEE International Conference on Computer Vision. IEEE, Kerkyra, Greece, pp. 307–314.

Laurentini, A., 1994. The visual hull concept for silhouette-based image understanding. IEEE Trans. Pattern Anal. Mach. Intell. 16 (2), 150–162.

Lewiner, T., Lopes, H., Vieira, A.W., Tavares, G., 2003. Efficient implementation of marching cubes' cases with topological guarantees. J. Graph. Tools 8 (2), 1–15.

Lin, C.-H., Kong, C., Lucey, S., 2018. Learning efficient point cloud generation for dense 3D object reconstruction. In: AAAI Conference on Artificial Intelligence (AAAI). Vol. 32.

Longuet-Higgins, H.C., 1981. A computer algorithm for reconstructing a scene from two projections. Nat. 293 (5828), 133–135.

Lorensen, W.E., Cline, H.E., 1987. Marching cubes: A high resolution 3D surface construction algorithm. ACM SIGGRAPH Comput. Graph. 21 (4), 163–169.

Madani, S., Amirfazli, A., 2014. Oil drop shedding from solid substrates by a shearing liquid. Colloids Surf. A: Physicochem. Eng. Asp. 441, 796–806.

Masuk, A.U.M., Salibindla, A., Ni, R., 2019. A robust virtual-camera 3D shape reconstruction of deforming bubbles/droplets with additional physical constraints. Int. J. Multiph. Flow 120, 103088.

Maurer, T., Mebus, A., Janoske, U., 2016. Water droplet motion on an inclining surface. In: 3rd International Conference on Fluid Flow, Heat and Mass Transfer, Ottawa, Canada, May 2-3.

Meagher, D., 1982. Geometric modeling using octree encoding. Comput. Graph. Image Process. 19 (2), 129–147.

Mescheder, L., Oechsle, M., Niemeyer, M., Nowozin, S., Geiger, A., 2019. Occupancy networks: Learning 3D reconstruction in function space. In: 2019 IEEE/CVF Conference on Computer Vision and Pattern Recognition (CVPR). IEEE, pp. 4455–4465.

Mildenhall, B., Srinivasan, P.P., Tancik, M., Barron, J.T., Ramamoorthi, R., Ng, R., 2020. NeRF: Representing scenes as neural radiance fields for view synthesis. In: Computer Vision – ECCV 2020. Springer International Publishing, Cham, pp. 405–421.

Minor, G., Djilali, N., Sinton, D., Oshkai, P., 2009. Flow within a water droplet subjected to an air stream in a hydrophobic microchannel. Fluid Dyn. Res. 41 (4), 045506.

Minor, G., Oshkai, P., Djilali, N., 2007. Optical distortion correction for liquid droplet visualization using the ray tracing method: Further considerations. Meas. Sci. Technol. 18, L23.

Newell, A., Yang, K., Deng, J., 2016. Stacked hourglass networks for human pose estimation. In: Computer Vision – ECCV 2016. In: Lecture Notes in Computer Science, Vol. 9912, Springer International Publishing, Cham, pp. 483–499.

Niemeyer, M., Mescheder, L., Oechsle, M., Geiger, A., 2020. Differentiable volumetric rendering: Learning implicit 3D representations without 3D supervision. In: 2020 IEEE/CVF Conference on Computer Vision and Pattern Recognition (CVPR). IEEE, pp. 3501–3512.

Park, J.J., Florence, P., Straub, J., Newcombe, R., Lovegrove, S., 2019. DeepSDF: Learning continuous signed distance functions for shape representation. In: 2019 IEEE/CVF Conference on Computer Vision and Pattern Recognition (CVPR). IEEE, pp. 165–174.

Raissi, M., Perdikaris, P., Karniadakis, G.E., 2019. Physics-informed neural networks: A deep learning framework for solving forward and inverse problems involving nonlinear partial differential equations. J. Comput. Phys. 378, 686–707. http://dx.doi.org/10.1016/j.jcp.2018.10.045.

Ríos-López, I., Karamaoynas, P., Zabulis, X., Kostoglou, M., Karapantsios, T.D., 2018. Image analysis of axisymmetric droplets in wetting experiments: A new tool for the study of 3D droplet geometry and droplet shape reconstruction. Colloids Surf. A: Physicochem. Eng. Asp. 553, 660–671.

Saito, S., Huang, Z., Natsume, R., Morishima, S., Kanazawa, A., Li, H., 2019. PIFu: Pixel-aligned implicit function for high-resolution clothed human digitization. In: Proceedings of the IEEE/CVF International Conference on Computer Vision (ICCV).

Schleizer, A.D., Bonnecaze, R.T., 1999. Displacement of a two-dimensional immiscible droplet adhering to a wall in shear and pressure-driven flows. J. Fluid Mech. 383, 29–54.

Seevaratnam, G.K., Ding, H., Michel, O., Heng, J., Matar, O.K., 2010. Laminar flow deformation of a droplet adhering to a wall in a channel. Chem. Eng. Sci. 65 (16), 4523–4534.

Shorten, C., Khoshgoftaar, T.M., 2019. A survey on image data augmentation for deep learning. J. Big Data 6 (1), 60. http://dx.doi.org/10.1186/s40537-019-0197-0.

Shrivastava, A., Pfister, T., Tuzel, O., Susskind, J., Wang, W., Webb, R., 2017. Learning from simulated and unsupervised images through adversarial training. In: 2017 IEEE Conference on Computer Vision and Pattern Recognition (CVPR). pp. 2242–2251.

Taubin, G., 1995. Curve and surface smoothing without shrinkage. In: Proceedings of IEEE International Conference on Computer Vision. IEEE Comput. Soc. Press, Cambridge, MA, USA, pp. 852–857.

Theodorakakos, A., Ous, T., Gavaises, M., Nouri, J.M., Nikolopoulos, N., Yanagihara, H., 2006. Dynamics of water droplets detached from porous surfaces of relevance to PEM fuel cells. J. Colloid Interface Sci. 300 (2), 673–687.

Thompson, L., 1994. The role of oil detachment mechanisms in determining optimum detergency conditions. J. Colloid Interface Sci. 163 (1), 61–73.

Thoreau, V., Malki, B., Berthome, G., Boulange-Petermann, L., Joud, J.C., 2006. Physico-chemical and dynamic study of oil-drop removal from bare and coated stainless-steel surfaces. J. Adhes. Sci. Technol. 20 (16), 1819–1831.

Tieleman, T., Hinton, G., 2012. Lecture 6.5-rmsprop: Divide the gradient by a running average of its recent magnitude. COURSERA: Neural Netw. Mach. Learn. 4 (2), 26–31.

Tomiyama, A., Celata, G.P., Hosokawa, S., Yoshida, S., 2002. Terminal velocity of single bubbles in surface tension force dominant regime. Int. J. Multiph. Flow 28 (9), 1497–1519.

Wang, X., Xu, B., Chen, Z., Del Col, D., Li, D., Zhang, L., Mou, X., Liu, Q., Yang, Y., Cao, Q., 2022. Review of droplet dynamics and dropwise condensation enhancement: Theory, experiments and applications. Adv. Colloid Interface Sci. 305, 102684.

Wang, N., Zhang, Y., Li, Z., Fu, Y., Liu, W., Jiang, Y.-G., 2018. Pixel2Mesh: Generating 3D mesh models from single RGB images. In: Computer Vision – ECCV 2018. In: Lecture Notes in Computer Science, Vol. 11215, Springer International Publishing, Cham, pp. 55–71.

Westermann, R., Kobbelt, L., Ertl, T., 1999. Real-time exploration of regular volume data by adaptive reconstruction of isosurfaces. Vis. Comput. 15 (2), 100–111.

Wu, J., Zhang, C., Xue, T., Freeman, W.T., Tenenbaum, J.B., 2016. Learning a probabilistic latent space of object shapes via 3D generative-adversarial modeling. In: Proceedings of the 30th International Conference on Neural Information Processing Systems. NIPS '16, Curran Associates Inc, Red Hook, NY, USA, pp. 82–90.

Youngs, D., 1982. Time-dependent multi-material flow with large fluid distortion. In: K.W., M., M.J., B. (Eds.), Numerical Methods for Fluid Dynamics. Vol. 24, Academic Press, New York, pp. 273–285.

Zhang, X., Tuna, B.A., Yarusevych, S., Peterson, S.D., 2021. Flow development over isolated droplet-inspired shapes. Int. J. Heat Fluid Flow 88, 108756.

Zhi-yong, L., Xiao-feng, P., Wang, X.-D., 2006. Oscillation characteristics of droplets on solid surfaces with air flow. Heat Transf.— Asian Res. 35, 13–19.